In-orbit calibration of the XMM-Newton telescopes

Ph. Gondoin[a], B. Aschenbach[b], C. Erd[a], D.Lumb[a], S. Majerowicz[c]
D. Neumann[c], J.L.Sauvageot[c]

[a] European Space Research and Technology Center, 2200 AG Noordwijk zh, the Netherlands

[b] Max-Planck Institute fur Extraterrestrische Physik, 8046 Garching, Germany

[c] Commissariat a l'Energie Atomique, 91191 Gif-sur-Yvette cedex, France

ABSTRACT

The High Throughput X-ray Spectroscopy Mission XMM−Newton of the European Space Agency (ESA) was launched on December 10 1999 by an Ariane V rocket. The satellite observatory uses three grazing incidence telescopes coupled to reflection grating spectrometers and x-ray CCD cameras. Each x-ray telescope consists of 58 Wolter I mirrors which are nested in a coaxial and cofocal configuration. The XMM−Newton Science Operation Center has completed a coherent programme for the in-orbit calibration and performance verification of the x-ray observatory. This paper presents first measurement results of the x-ray telescopes image quality and effective area obtained during this campaign.

Keywords: XMM−Newton, x-ray astronomy, Wolter I telescope, grazing incidence optics

1. INTRODUCTION

On December 10 1999 the XMM-Newton space observatory was placed in a 48 hours orbit by the first commercial Ariane V launcher. The High Throughput X-ray Spectroscopy Mission XMM-Newton[1] is a "Cornerstone" project in the ESA long-term programme for space science. Its primary objective is to perform high throughput spectroscopy of cosmic x-ray sources over a broad band of energies ranging from 0.1 keV to 10 keV down to a limiting flux of 10^{-15} ergs s^{-1} cm^{-2}. The XMM-Newton payload includes:

- 3 grazing incidence telescopes[2] which provide an effective area higher than 4000 cm^2 at 2 keV and 1600 cm^2 at 8 keV and an image quality better than 15 arcsec Half Energy Width (HEW),
- 3 CCD imaging cameras (EPIC)[3,4], one at the prime focus of each telescope, which provide imaging in a 30 arcmin field of view and broadband spectroscopy with a resolving power of between 5 and 60 in the energy band 0.1 to 15 keV,
- 2 reflection grating spectrometers (RGS)[5] which provide spectroscopy between 0.2 and 2 keV with a resolving power of over 250 at 0.5 keV,
- 1 optical monitor (OM)[6] which permits simultaneous monitoring of x-ray sources in the UV and optical range included between 1600 and 6000 Angströms.

In response to the first XMM−Newton Announcement of Opportunity (AO1), observation proposals of a large number of professional astronomers worldwide were received which exceed by a large amount the available observing time. The very high throughput of the x-ray telescopes combined with the spectroscopic performance of the EPIC and RGS instruments provide forefront capabilities to study hot astrophysical plasma having temperatures in the range 10^6 to 10^8 K. These sources radiate the bulk of their energy in the form of continuum and line emissions at x-ray wavelengths included between 0.8 Angström (15 keV) and 120 Angström (120 eV). The interpretation of this new generation data requires that calibration of the telescopes and payload is performed to a high level of accuracy. For instance, in order to derive differential emission measure distributions of optical thin plasmas as a function of temperature, as well as for deriving elemental abundances or electron densities, relative line intensities and the continuum have to be measured with an accuracy of 5 to 10 percents. The XMM−Newton Science Operation Center in coordination with the Instruments Teams has completed a coherent programme for the in-orbit calibration and performance verification of the x-ray observatory. This paper presents first measurements results of the telescopes image quality and effective area obtained during this calibration campaign.

2. DESCRIPTION OF THE X-RAY TELESCOPES

A Wolter I design was selected[7] for each of the three XMM-Newton telescopes. This design was driven by the requirement of obtaining the highest possible effective collecting area over a wide band of energies. Particular emphasis has been given on the region around 7 keV, in which the K lines of the astrophysically important iron appear. Because of this high energy requirement the mean mirror grazing incidence angle is limited to 30 arcmin. The total length of the telescope was imposed by the launcher so that the focal length is 7.5 meters. Similarly, the maximum diameter of each of the three adjacent telescopes could not exceed 70 cms to be compatible with the shroud diameter of the launcher.

Development work on the mirrors started with the development of carbon reinforced plastics (CFRP) mirrors by epoxy replication from master mandrel polished to x-ray imaging quality. This technique produced lightweight mirrors of high stiffness. However, the non-amorphous structure of CFRP induced printthrough of the CFRP laminate through the resin due to moisture outgassing of the epoxy under vacuum[8]. Hence, a replica technique by electroforming nickel mirrors from superpolished mandrels was finally selected following the succesful results obtained for the SAX and Jet-X telescopes[9]. Based on mass constraints and on the performance of the Nickel electroforming technology, a 0.47 mm wall thickness for the smallest mirror diameter of 300 mm was baselined. The thickness variation then increases linearly with shell diameter in order to guarantee sufficient stiffness. The thickness of the 700 mm diameter mirror equals 1.07 mm. A minimum radial separation of 1 mm between adjacent shells was adopted. Each mirror shell of the three Wolter telescopes consists of a paraboloid and an associated hyperboloid which are replicated together in one piece in order to facilitate alignment and integration. Since the effective collecting area decreases with smaller shell radius, the inner shells become less and less effective and the associated throughput gain had to be traded against the effort of production. An optimum at 8 keV is reached for an innermost shell diameter of 150 mm and a total of 58 shells per module.

Table 1. Optical characteristics of an XMM−Newton telescope

focal length	7500 mm
outer mirror radius	350 mm
inner mirror radius	153 mm
axial mirror length	600 mm
outer mirror thickness	1.07 mm
inner mirror thickness	0.47 mm
minimum packing distance	1 mm
mirror substrate material	Nickel
reflective coating	Gold
number of mirrors per module	58

The 58 Wolter I mirrors of each telescope are bounded on their entrance aperture to the 16 spokes of a single spider[10] (see Fig.1). The spider is connected to the support platform of the spacecraft via an interface structure consisting on an outer cylinder and an interface ring. The outer cylinder is prolongated by an adaptor ring which connects the mirror module to an exit thermal baffle. On two of the three telescopes, this adaptor ring also interface the mirror module to a reflection grating assembly (see Fig.2) which diffracts part of the telescope exit beam onto a strip of 9 CCD detectors. An electron deflector is located in the exit aperture of the mirror module before the grating assembly. It consists of a sixteen spoke spider carrying magnets. These produce a circumferential magnetic field which prevents soft energy electrons reflected by the mirrors to reach the focal plane detectors. Two sieve plates consisting each of 58 annular apertures are located respectively 79 and 150 mm in front of the mirror entrance aperture. The two sieves x-ray baffle acts as a collimator and considerably reduces the amount of straylight in the field of view of the EPIC cameras placed at the prime focus of each telescope.

The telescopes and x-ray baffles were built by industry including Medialario (Italy), Carl Zeiss (Germany), Kayser-Threde (Germany) and Sener (Spain). Throughout the development, manufacturing and on-ground calibration

programmes, extensive x-ray and EUV tests were performed at the X-ray test facility PANTER of the Max-Planck-Institut fur Extraterrestrische Physik[11] and at the Focal-X facility of the Centre Spatial de Liege in Belgium[12].

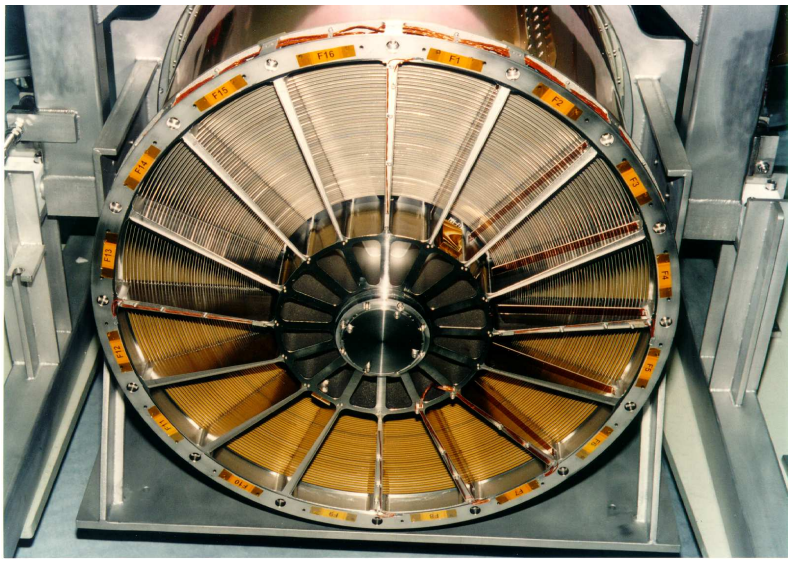

Figure 1. Entrance aperture of an XMM−Newton x-ray telescope

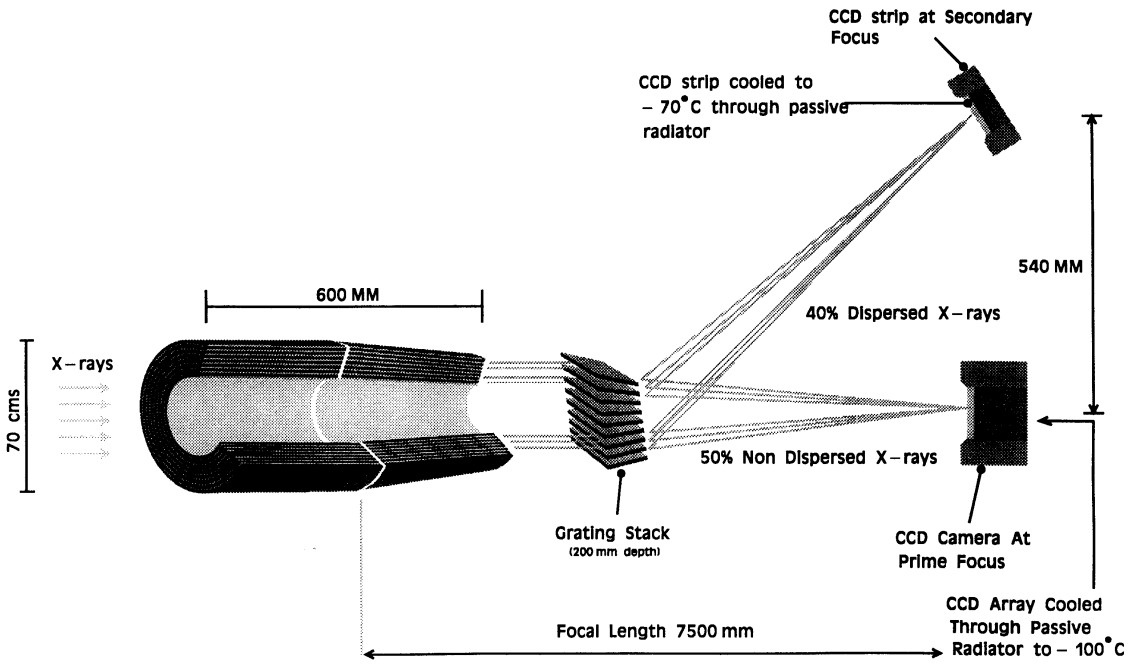

Figure 2. Optical combination of an x-ray telescope with the RGS and EPIC experiments

3. CALIBRATION OVERVIEW

The open stellar cluster NGC 2516 (see Fig.3) was observed by the EPIC cameras for the purpose of boresight and plate scale calibration of the x-ray telescopes. More than hundred stars were detected. Fig. 3 shows that the sources in average are brighter close to the center of the field of view. This illustrates the vignetting effect of the telescopes and x-ray baffles combination. Also, the image response to the individual point sources varies significantly over the field of view due to geometrical off-axis aberrations induced by the grazing incidence optics. These instrumental effects induced by the telescopes in the image formation process are described by the following expression.

$$I(x,y,E) = A_{eff}(x,y,E).PSF(x,y,E) \otimes O(x,y,E)$$

where O(x,y,E) and I(x,y,E) are the brightness distributions in the object and in the image respectively. PSF(x,y,E) and A_{eff}(x,y,E) describe the Point Spread Function (PSF) and the effective collecting area of the XMM−Newton telescopes as a function of photon energy and field position. A calibration of these instrumental functions is needed for the analysis of EPIC raw dataset by the XMM Science Analysis Software (SAS) e.g. for the purpose of source detection or filtering, selection of photometric extraction windows, background substraction, detector pile-up correction, absolute flux determination or image restoration. The on-axis effective area of the x-ray telescopes also affects the spectral sensitivity of the two Reflection Grating Assemblies (RGA) in the wavelength range included between 5 and 40 Angströms. At long wavelengths (see Fig.4), the line spread function of the RGA x-ray spectrometer is determined by the telescope point response. Hence, the telescopes PSFs and effective areas are major contributors to the EPIC and RGA instrumental responses R(I,E) which relate count rates C(I) measured in the instrument channels to actual spectra S(E) of astrophysical sources.

$$C(I) = \int_0^\infty S(E).R(I,E).dE$$

The absence of cosmic x-ray sources which can serve as in-orbit calibration standards prevents an in-flight calibration of the telescopes to a high level of accuracy. The effective area and point spread function of the mirrors were therefore characterized on-ground during an extensive calibration campaign[13,14]. The situation was however complicated since on-ground testing could not be performed in fully representative operation conditions. Indeed, full aperture x-ray test data gathered at the MPE long beam Panter Facility were compromised by the finite source distance. In such tests a large fraction of the reflecting surfaces of the mirror shells were not used. Full aperture data for a source at infinity is available from the CSL vertical test facility but only at EUV wavelengths. In order to overcome these difficulties and to satisfy the calibration requirements, a comprehensive numerical model of the XMM mirror system was built[15,16]. This model has been used to generate the initial telescope calibration database by extrapolating on-ground tests to in-orbit operation conditions and by interpolating between the finite number of measurement points. The major objective of the in-orbit calibration of the x-ray telescope is to validate this initial database using observation data of appropriate celestial targets.

The in-orbit calibration activities include the determination of the instrument boresight and plate scale, the characterization of the telescope PSF, effective area and vignetting function and the quantification of the observatory straylight rejection efficiency. A summary list of celestial sources which were observed for that purpose is given in Table 2. Calibration of the relative pointing offset and plate scale of the different telescopes is performed using EPIC observations of open stellar clusters (see Fig.3). Open clusters allow the simulaneous detection of a large number of x-ray sources having optical counterparts with well known positions. Characterization of the telescope PSF is performed using x-ray sources bright enough to image the wing of the telescope PSF but with a count rate not exceeding a few counts per seconds to avoid detector pile-up effects. The absence of contamination effect during the launch and telescope tube outgazing phase can be verified by inspecting spectral regions close to the C K and O K absorption edges and by assessing the mirror reflectivity close to the Au M absorption edges. Lineless spectra of BL LAC objects were recorded for that purpose. The telescope vignetting functions are measured by observing supernovae remnants (SNRs) and bright Abell-type clusters of galaxies at different off-axis angles. The x-ray straylight rejection efficiency of the telescope baffles is quantified by pointing in the vicinity of the Crab Nebula, one of the x-ray brightest object in the sky.

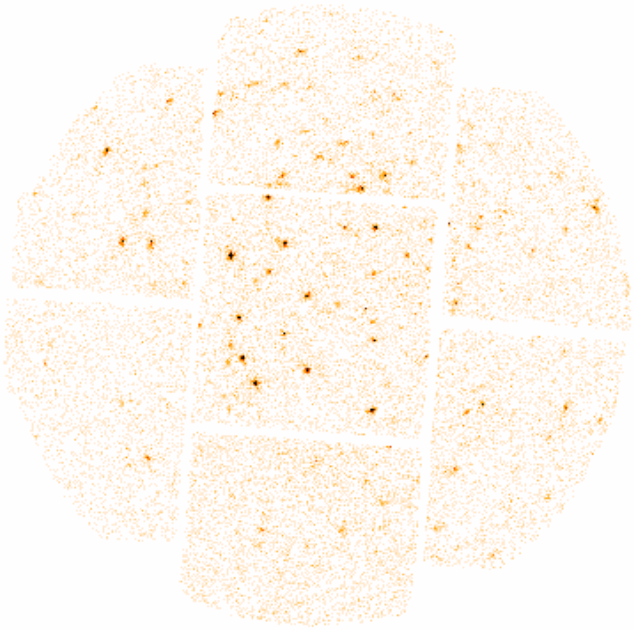

Figure 3. NGC 2516 open stellar cluster observed with the MOS 1 camera at the focus of the FM3 telescope

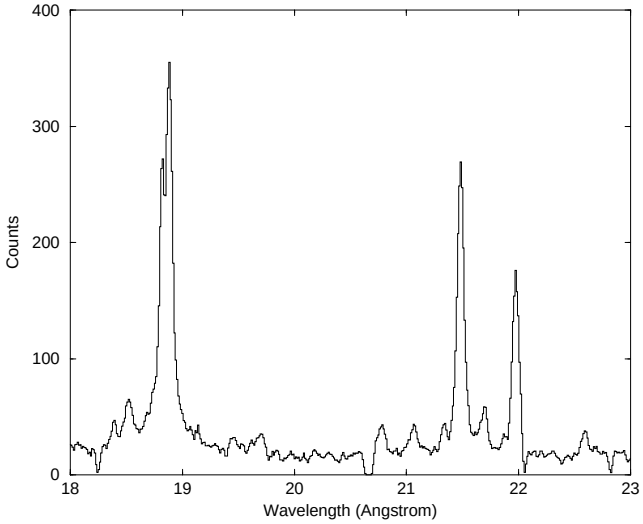

Figure 4. Capella spectrum obtained with the RGS spectrometer behind the FM3 telescope

4. IMAGE QUALITY

The FM3 and FM4 flight model telescopes are each associated with one RGS spectrometer and one EPIC MOS camera (see Fig.2). The third telescope, called the FM2 flight model, operates with one EPIC pn camera. Characterization of the telescope PSF requires the observation of bright x-ray point sources. However, EPIC CCDs operate in a photon counting mode which enables spectro-imaging by counting the number of photo-electrons produced in individual pixels. At high fluxes, photon pile-up, i.e., the arrival of more than one x-ray photon in a single pixel during one CCD frame period, effects the spectral response of EPIC and the telescope PSF measurements. Multi-pixel photon patterns can be created which are mis-identified as spurious events or cosmic rays and rejected by the onboard event reconstruction software of the MOS camera. In the full window mode of the EPIC MOS cameras, the 600 x 600 pixels of each of the seven CCDs are read every 2.6 seconds. To avoid pile-up, the source count rate must not exceed one

Table 2. Calibration targets of the XMM-Newton telescopes

Calibration	Target Name	Source Type	Exposure (ksec)
Alignment, boresight Plate scale	NGC 2516	Open stellar cluster	24
PSF	PKS0558-50 PKS0312-770 YY Gem	Active Galactic Nucleus Quasar Stellar corona	Com. 36 63
Imaging (deconvolution)	1ES0102 N132D	Supernova remnant Supernova remnant	19 24
Effective area (absorption edges)	MS1229.2+6430 MS0737+74	BL Lac object (AGN) BL Lac object (AGN)	54 69
Effective area (vignetting)	A 496 3C 58 G21.5-0.9	Cluster of galaxies Supernova remnant Supernova remnant	3 x 14 2 x 29 5 x 35
X-ray straylight	Crab Nebula	Supernova remnant	2 x 3
Visible straylight	Canopus	Bright star	

count per second. Hence, the achievable ratio signal to noise in the wing of the telescope PSF is limited. Fig.5 shows the PSF at low energy (E < 3 keV) of the FM4 telescope obtained after a 36 ksec observation of the PKS0312-770 quasar performed with the MOS2 camera operating in full frame mode. Due to the count rate limitation, the wings of the PSF are affected by a background contribution. However, Fig.5 demonstrates that the radial energy distribution in the central part of the PSF measured in-orbit is identical to CCD measurements performed on-ground at the PANTER test facility.

The relative background contribution can be reduced by measuring the telescope PSF on brighter sources and operating the EPIC cameras in small window mode. In such a mode, only part of the central CCD is read-out at a higher rate. Larger fluxes can be accommodated without photon pile-up. Such measurements of the on-axis telescope PSFs were performed using observations of the LMC X-3 and PKS 0558-504 sources in window mode[17]. The results are presented in Table 3. The pixel sizes of the MOS and pn EPIC CCDs are 40 μ and 150 μ respectively. These values correspond to 1.10 arcsec and 4.13 arcsec onto the sky to be compared with the 4-6 arcsec PSF Full Width Half Maximum (FWHM) measured on-ground. Hence, the pn camera only provides an upper estimate of the width of the FM2 telescope PSF core. The higher spatial sampling of the MOS CCDs allows a more accurate comparison between in-orbit and on-ground measurements of the FM3 and FM4 telescope PSFs. In the small window mode, the field of view of the central CCD of each camera is limited to less than 2 x 2 arcmin. Hence, the background contribution cannot be accurately subtracted and the encircled energy function in large extraction windows cannot be determined.

Within the above limitation, Table 3 confirms that the energy distribution in the telescope PSF measured in-orbit is identical to the on-ground calibration measurements. The EPIC cameras are in-focus and the figuring of

Table 3. On-ground and in-obit image quality measurements of the three x-ray telescopes on board XMM-Newton

	1.5 keV	1.5 keV	1.5 keV	1.5 keV	8.0 keV	8.0 keV	8.0 keV	8.0 keV
Telescope	in-orbit FWHM (arcsec)	on-ground FWHM (arcsec)	in-orbit HEW (arcsec)	on-ground HEW (arcsec)	in-orbit FWHM (arcsec)	on-ground FWHM (arcsec)	in-orbit HEW (arcsec)	on-ground HEW (arcsec)
FM2−pn	<12.5	6.6	15.2	15.1	<12.5	6.6	15.0	14.8
FM3−MOS1	4.3	6.0	13.8	13.6		5.1		12.5
FM4−MOS2	4.4	4.5	13.0	12.8		4.2		12.2

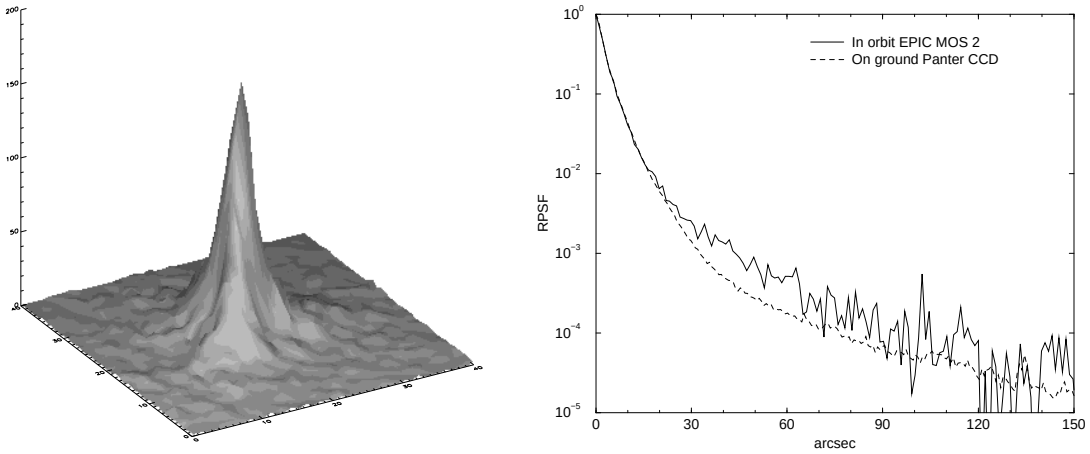

Figure 5. PSF of the FM4 telescope measured with the MOS 2 camera operating in full frame mode.

the mirrors was not affected by launch loads or gravity release effects. On ground calibration measurements of the telescopes PSFs can be confidently used for the analysis of data acquired in-orbit. Hence, a library of PSF calibration files has been generated by the science simulator at a set of discrete energies and off-axis angles. The simulator used telescope model files validated by the on-ground calibration measurements. The XMM−Newton Science Analysis Software (SAS) can access the PSF calibration files through a layer of calibration routines which calculate brightness distribution and encircled energy functions for any field angle and spectral energy range accessible to the EPIC cameras.

At energy below about 4 keV, the PSFs of the XMM−Newton telescope are energy independent and stationary within a 10 x 10 arcmin field of view corresponding to the central EPIC MOS CCDs. Within this spatial and spectral domain, the telescope PSF can be described by an analytical expression using a single set of fitting parameters. Specially, a combination of three Gaussians provides an accurate description of the x-ray telescope PSFs.

$$PSF(x,y) = \sum_{i=1}^{2} a_{1i} e^{-(b_{1i}(x-c_{1i})^2 + b_{2i}(x-c_{2i})^2)} (1 + b_{3i} cos(3.\theta + b_{4i})) + a_{13} e^{-(b_{13}(x-c_{13})^2 + b_{23}(x-c_{23})^2)} (1 + b_{33} cos(16.\theta + b_{43}))$$

With such an expression, low χ^2 with respect to on-ground EUV observation at the CSL facility have been achieved using fitting routines based on the conjugate gradient method[18]. The first two Gaussians describe the PSF core broadening by tiny mirror misalignment effects and the PSF feet generated by figuring errors at low spatial frequencies which produce slope errors in the few arcseconds range. The broadest Gaussian describe the wing of the PSF due to slope errors at higher spatial frequencies close to the mirror edges. This contribution to the PSF wings is superseded at high photon energy by surface scattering effects[19]. A three fold azimuthal modulation has been added to the first two Gaussians which simulates the triangular shape of the FM4 PSF (see Fig.5) induced by the non-perfect flatness of its spider. A sixteen fold azimuthal modulation is applied to the broad Gaussian to map the star like brightness distribution produced by the 16 arms spiders.

The PSF parametrisation by Gaussian functions is of special interest for deconvolving EPIC images using algorithms based on Fourier transforms. Such algorithms restore low contrasts in images of bright sources with diffused extended emissions. As an example, Fig.6 (top left) shows an EPIC MOS 1 image of the supernova remnant E0102-70 located in the Small Magellanic Cloud. The angular diameter of this type II SNR resulting from the explosion of a massive star about 1000 years ago is 40 arcsec. This has to be compared with the on-axis Point Spread Functions (PSF) of the XMM-Newton telescopes at low energy which exhibit narrow cores (FWHM = 4 arcsec) and broad wings (90 % Energy Width = 60 arcsec) typical of X-ray grazing incidence optics. The E0102-70 raw image was

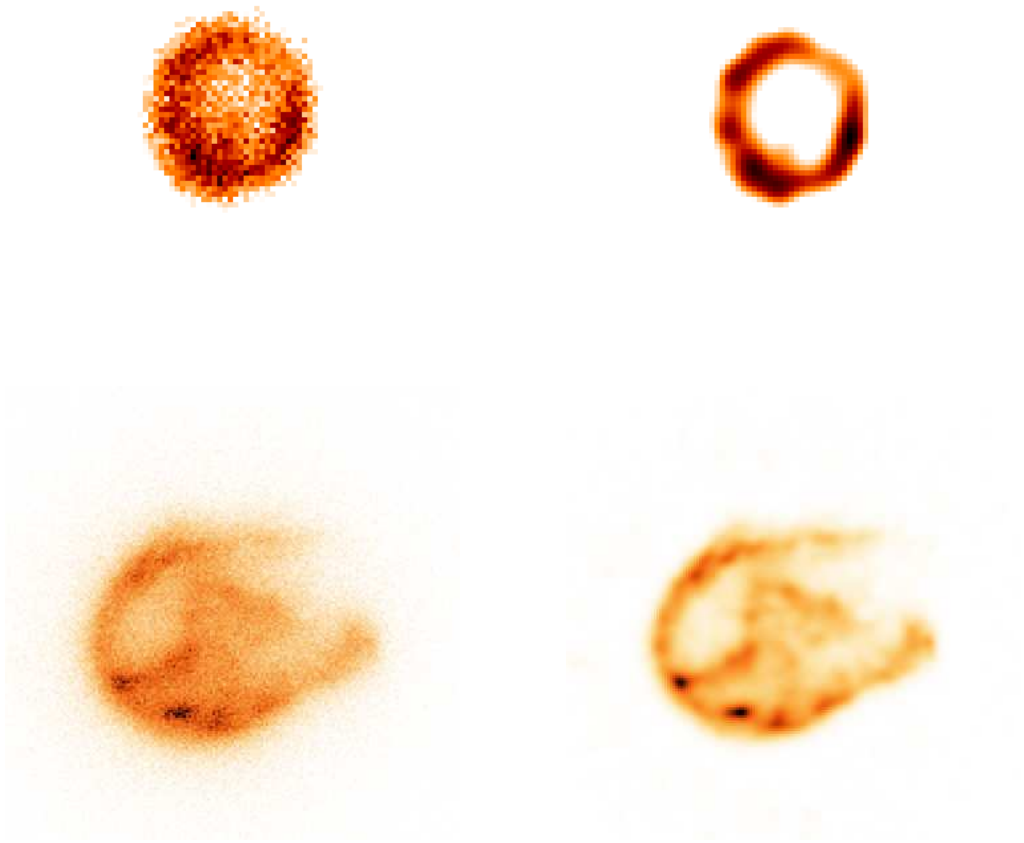

Figure 6. FM3 images of SNRs E0102-70 (up) and N132D (bottom) before (left) and after (right) deconvolution.

deconvolved by the three Gaussian parametrisation of the FM3 telescope PSF using a Maximum Likelihood solution for the restoration of blurred images with additive noise. The deconvolved image (Fig.6 top right) reveals that the x-ray emission from the multimillion degree shocked material is concentrated in a thick ring with sharp edges. The deconvolved image also shows bright blobs indicating that the ejecta material pushing into the interstellar gas is breaking into clumps dispersing heaving elements into space.

Fig.6 (bottom) shows an other example of a raw (left) and deconvolved (right) EPIC MOS 1 image of a supernovae remnant. N132D is also a type II SNR resulting from the explosion of a massive progenitor star in the Large Magellanic Cloud . Its diameter is about 80 arcsec and its age estimated to 1300 years is similar to that of E0102-70. However, the deconvolved image of N132D reveals a more complexe spatial structure. An outer shell with sharp edges is visible but an extended region of diffuse emission with filament structures is also present. These two examples illustrate how the characterization of the XMM-Newton telescopes PSFs enable to study extended object such as supernova remnants and clusters of galaxies with a spatial resolution close to the 4−5 arcsec FWHM of the PSFs cores.

5. EFFECTIVE AREA

Fig.7 (left) shows the effective area of the XMM telescopes with and without the RGA grating assemblies. This calibration curve has been calculated by the science simulator using a numerical model of the XMM mirror systems validated by on-ground calibration tests. The telescope model simulates the reflection efficiency of the mirrors and

the vignetting effect by the telescope structure. The effective area is calculated by ray-tracing incident photons taking into account the figuring errors and surface roughness of the mirrors. Their gold surface reflectivity is calculated from tables of refraction indices using the Fresnel equation for a semi-infinite medium. The 1993 Henke table[20] was used initially as updated by Gullikson based on new absorption coefficient data to improve the description of the gold M absorption edge. The numerical model was then tuned based on the results of on-ground x-ray pencil beam and full aperture illumination tests performed at the CSL and PANTER facilities. The simulation results indicated a 3 percent calibration accuracy of the effective area on-axis over most of the XMM spectral range. A possible exception, however, is the gold M absorption edge due to the use of discrete spectral lines for effective area measurements.

Within the in-flight calibration programme, bright BL Lac objects with hard spectra were observed to obtain continuum emission spectra in the 2.2 to 3.4 keV range of the Au M absorption edges. According to a standard model, BL LAC objects are Active Galactic Nuclei (AGNs) with relativistically beamed jets very close to the line of sight. They emit an intense synchrotron radiation which is observed through several decades in frequencies. This lineless continuum emission is well suited to map the edge discontinuities of the telescopes and instruments effective area. Fig.7 (right) shows spectra of the MS1229.2+6430 BL Lac object obtained with the MOS cameras through thin Al filters. These spectra were fitted with single power law models plus a photo-electric absorption. A well constrained fit with a reduced χ^2=1.03 was obtained using a 2.34 powerlaw photon index and a 2.87 10^{20} cm^{-2} hydrogen column density. The fit were performed using the XSPEC software package in combination with response matrix files identical for the two MOS cameras. These response files include effective area calibration files of the x-ray telescopes. An important result is that no excess residuals to the fitting curve are observed around the 2.2 keV location of the Au M edge.

One concern regarding calibration was the transfer accuracy of on-ground calibration data to in-orbit operation. Aside from the difficulties to perform on-ground tests in representative operation condition, it was feared that calibration accuracy could be limited by any contamination occured after on-ground testing. For some payload elements, two years elapsed between on-ground effective area calibration and start of in-orbit operation. Contaminants mainly consist of dust, hydro-carbons and water. Hence, it is worth mentioning that no significant residuals to the fit of MS1229.2+6430 spectra were observed at the C K (284 eV) and O K (532 eV) edges location.

The above results concerning the effective area close to the Au M edge and the absence of contamination are encouraging. Nevertheless, spectra with higher signal to noise ratio obtained e.g by co-adding different observations are needed to verify the in-orbit calibration of the relative effective area with the requested accuracy.

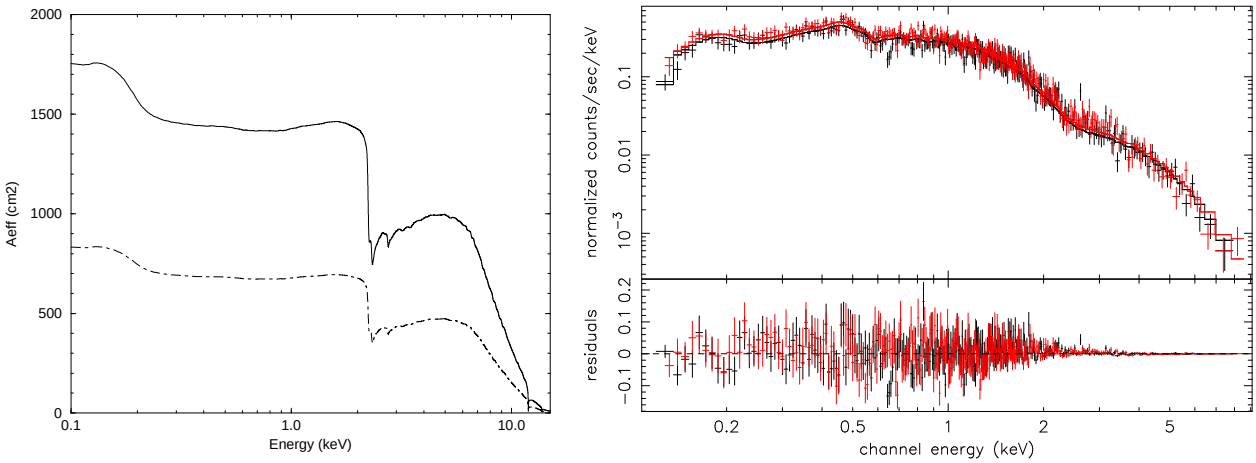

Figure 7. Left: on-axis effective area of the XMM telescopes without (solid line) and with (dot-dashed line) the Reflection Grating Assembly (RGA). Right: MOS 1 and 2 spectra of the MS1229.2+6430 BL Lac object including spectral fit residuals to a power law model with an absorbed column density.

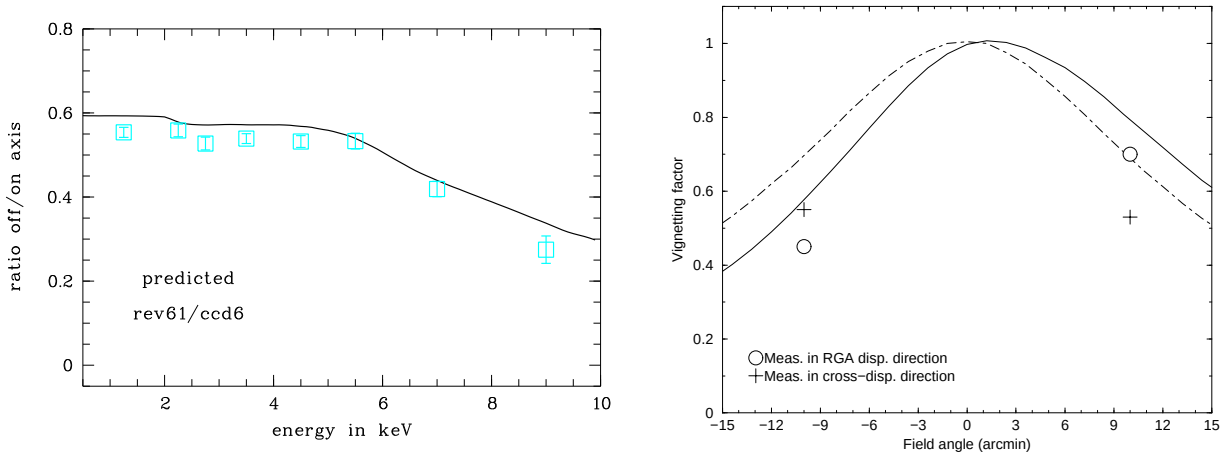

Figure 8. FM3 telescope vignetting measurements using G21.5-0.9 SNR observations compared with vignetting curves calculated using the science simulator. Left: energy dependence of the vignetting function at a 10 arcmin off-axis angle perpendicular to the grating dispersion direction. Right: angle dependence of the vignetting function below 4.5 keV in azimuths respectively parallel (continuous line) and perpendicular (dot-dashed line) to the RGA dispersion direction.

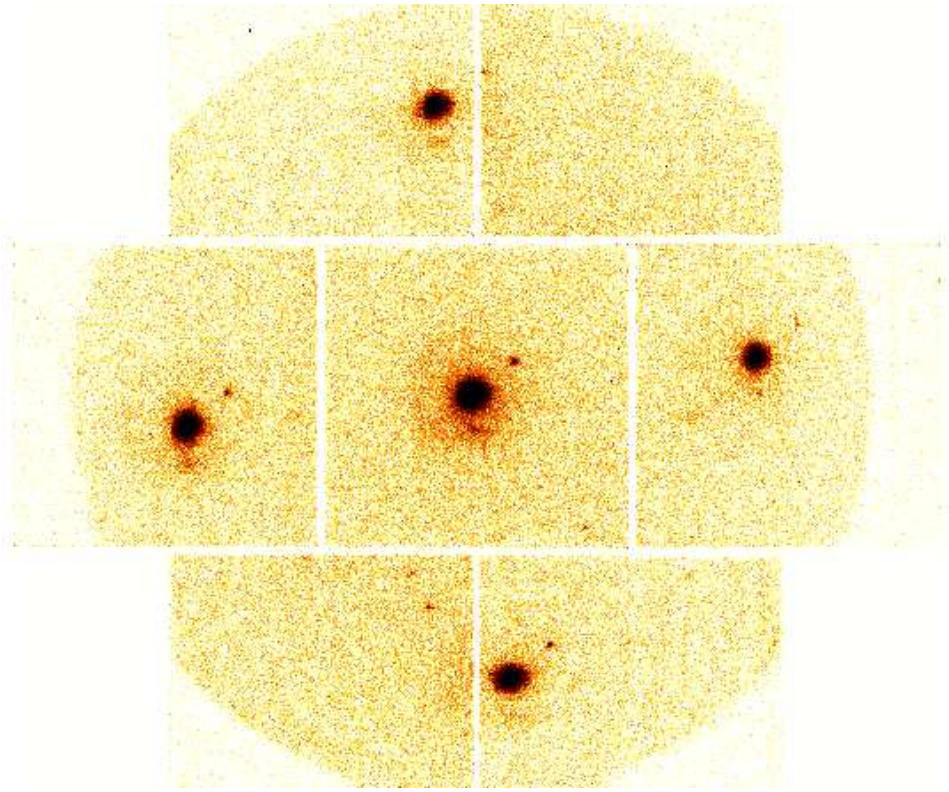

Figure 9. Co-added MOS2 offset images of the G21.5-0.9 supernovae remnant

In order to measure the effective area variation over the EPIC field of view, the G21.5-0.9 supernova remnant was observed on-axis and at four off-axis positions. Fig.9 shows a co-added image of the five MOS 1 observations. The 10 arcmin off-axis pointings in orthogonal direction were used to verify the azimuthal variation of the vignetting function produced by the RGA assemblies. Indeed, the stack of gratings located behind the FM3 and FM4 telescopes acts as a Venitian blind. Due to the grating plane inclination with respect to the telescope optical axis (see Fig. 2), the vignetting function in the EPIC detector plane is modulated azimuthaly with the highest effective area in the RGA dispersion direction.

In each MOS 1 observation datafile, counts were extracted within window of 40″ radius smaller than the image distances to the CCD edges. Due to off-axis geometrical aberrations and scattering effects, the telescope PSF changes across the EPIC field of view. The related variation of the number of counts within the selected extraction window was estimated to be less than 1% between on-axis and off-axis observations. As the telescope vignetting function is also energy dependent, x-ray events were splited into eight energy bands, namely 0.5–2.0 keV, 2.0–2.5 keV, 2.5–3.0 keV,3.0–4.0 keV, 4.00–5.0 keV, 5.0–6.0 keV, 6.0–8.0 keV and 8.0–10.0 keV. X-ray events below 0.5 keV were filtered out due to uncertainties on the CCD flatfields in this range. For each observation, background contribution was estimated within an annular region around the extraction window. After background subtraction, count rates were calculated for the different exposure times which range between 14 and 29 ksec. The vignetting function was finally determined as the ratio between on-axis and off-axis count rates.

Fig.8 (left) shows the energy dependence of the vignetting function at 10 arcmin in the azimuth perpendicular to the RGA dispersion direction. Error bars have been estimated applying Poisson statistics to the source and background counts. As calculated by the science simulator, the vignetting function at this field angle is energy independent till about 4.5 keV. The average vignetting measurememts below 4.5 keV are compared in Fig.8 (right) with vignetting curves generated by the science simulator. The measurements confirm the azimuthal modulation of the vignetting function. At 10 arcmin off-axis angle, they are within 14% of the simulator vignetting calculation. Although these preliminary measurements seem to be lower than expected, they constitute a good result in view of the complexity of the optical chain which include 2 baffle sieves, a telescope spider, 58 mirrors, a magnetic deflector, the grating box structure, 180 grating elements, a filter and 5 different CCDs.

6. CONCLUSIONS

The XMM−Newton Science Operation Center has completed a coherent programme for the in-orbit calibration of the XMM−Newton observatory. A fraction of the x-ray telescope calibration data, mostly MOS 1 camera measurements, has been analysed. The preliminary results tend to the following conclusions.

1. the telescopes point responses measured in-orbit are identical to on-ground calibration measurements with an half energy width smaller than 15 arcsec,
2. extended sources in the central part of the EPIC camera field of view can be studied with a spatial resolution comparable to the 4 arcsec full width half maximum of the telescope PSFs,
3. fitting residuals of BL Lac object spectra confirm the on-ground calibration of the relative effective area close to the Au M edges,
4. no evidence for contamination is detected close to the C K and O K edges,
5. measurements of the in-orbit vignetting function at 10 arcmin off-axis angles compare with simulation results extrapolated from on-ground calibration to better than 15%.

Furthermore, pointings in the vicinity of the Crab nebula demonstrate the high straylight rejection efficiency of the telescope x-ray baffles. These preliminary results indicate that the calibration of the telescope image quality and effective area performed on-ground can be transfered to in-orbit operation most likely without a significant loss of accuracy.

ACKNOWLEDGMENTS

We are grateful to our colleagues from the XMM−Newton Science Operation Center for their support in implementing the in-orbit calibration programme. Many thanks also go to the development team of the XMM−Newton Science Analysis Software.

7. REFERENCES

1 F. Jansen, "XMM: Advancing Science with the High-Throughput X-ray Spectroscopic Mission", ESA bulletin 100, pp.15-20, 1999.

2 Ph. Gondoin, D. de Chambure, K. van Katwijk, Ph. Kletzkine, D. Stramacicioni, B. Aschenbach, O. Citterio, R. Willingale, "The XMM Telescope", SPIE Proc.2279, pp.86-100, 1994.

3 A.D.Holland, M.J.L.Turner, A.F.Abbey, P.J. Pool, "MOS CCDs for the EPIC on XMM", SPIE Proc.2808, pp. 414-420, 1996.

4 N. Meidinger, H.W. Brauninger, R. Hartmann, G. Hartner, N. Krause, E. Pfeffermann, C. Reppin, G. Schwaab, L. Struder, J. Trumper, P. Holl, J. Kemmer, S. Krisch, H. Soltau, C. van Zanthier, D. Hauf, R. Richter, "PN-CCD detector for the European Photon Imaging Camera on XMM", SPIE Proc.2808, pp. 492-503, 1996.

5 A.C.Brinkman, H.J.M.Aaarts, A.J.F.den Boggende, L.Dubbeldam, J.W.den Herder, J.S.Kaastra, P.A.J.de Korte, R.Mewe, C.J.Hailey, S.M.Kahn, F.B.S.Paerels, G.Branduardi-Raymont, J.V.Bixler, K.Thomsen, A.Zehnder, "Reflection Grating Spectrometer on-board XMM", SPIE Proc.2808, pp. 463-480, 1996.

6 R. Much, D. Lumb, M.S. Cropper, R. Hunt, K.O. Mason, F.A. Cordova, T. Sasseen, C. Ho, W. Priedhorsky, C.Jamar, E. Antonello, "The Optival/UV Monitor on the X-ray Multi Mirror Mission",Proceedings of the Conference " Ultraviolet Astrophysics, Beyond the IUE Final Archive", Sevilla, Spain, ESA SP-413, p.815, 1998.

7 B.Aschenbach, O.Citterio, J.M. Ellwood, P.Jensen, P.de Korte, A.Peacock, R.Willingale," The High-Throughput Spectroscopic Mission",Report of the Telescope Working Group, Proc.ESA SP-1084, 1987.

8 Ph. Gondoin, K. van Katwijk, B. Aschenbach, N. Schulz, R. Borret, H. Glatzel, O. Citterio, R. Willingale," XMM Telescope Development", EOS/SPIE Proc. 2209, PP438-450, 1994.

9 O. Citterio, P. Conconi, M. Ghigo, F. Mazzoleni, H. Brauninger, W. Burkert, N. Schulz, P. Gondoin, K. van Katwijk, R. Laurance, "Results of x-ray Measurements on Electroformed Mirror Shells for the XMM Project", SPIE Proc. 1742, 1992.

10 Ph. Gondoin, B. Aschenbach, H. Brauninger, D. de Chambure, J.P. Colette, R. Egger, K. van Katwijk, D. Lumb, A. Peacock, Y. Stockmann, J.P. Tock, R. Willingale, "X-ray Performance of a Qualification Model of an XMM Mirror Module", SPIE Proc. 2908, p. 390, 1996.

11 B. Aschenbach, H. Bräuninger, K-H Stephan, J. Trümper," X-ray Test Facilities at Max-Planck Institut Garching", in Space Optics - Imaging X-ray Optics Workshorp, M. Weisskopf, ed., Proc. SPIE 184 pp. 234-238, 1979.

12 Y. Stockman, J.P. Tock, D. de Chambure, Ph. Gondoin, "XMM flight mirror module environmental and optical testing", SPIE Proc. 3114, p. 566, 1997.

13 Ph. Gondoin P., B. Aschenbach, M. Beijersbergen, R. Egger, F. Jansen, Y. Stockman, J.P. Tock," Calibration of the first XMM flight mirror module: I. Image quality", SPIE Proc. 3444, p. 278, 1998.

14 Ph. Gondoin P., B. Aschenbach, M. Beijersbergen, R. Egger, F. Jansen, Y. Stockman, J.P. Tock," Calibration of the first XMM flight mirror module: II. Effective Area", SPIE Proc. 3444, p. 290, 1998

15 C. Erd, F. Jansen, J. Brumfitt, M. Beijersbergen, Ph. Gondoin, H. Siddiqui, J. Bakker, P. Videler, L. Jalota, "Novel Use of a Simulator for the Calibrations of Scientific Instruments", Astronomical Data Analysis Software and Systems VIII, ASP Conference Series, Vol. 172. Ed. David M. Mehringer, Raymond L. Plante, and Douglas A. Roberts, p. 119, 1999.

16 Ph. Gondoin, B. Aschenbach , H. Brauninger , D. de Chambure, J.P. Colette, R. Egger, K. van Katwijk, D. Lumb, A. Peacock, Y.Stockmann, J.P. Tock, R. Willingale, " Simulation of the XMM Mirror Performance based on Metrology Data", SPIE Proc. 2808, pp. 390-401, 1996.

17 B. Aschenbach, U. Briel, F. Haberl, H. Bräuninger, W. Burkert, A. Oppitz, P. Gondoin, D. Lumb, in X-ray Optics, Instruments and Mission, J. Trümper and B. Aschenbach eds., Proc. SPIE, 2000.

18 Y. Stockman, Y. Houbrechts, Y. Naze, P. Rochus, J.P. Tock, Ph. Gondoin, "PSF modelling of the XMM Flight Mirror Modules", SPIE Proc. 3765, p. 265, 1999.

19 Ph. Gondoin, A. Freund, S. Gougeon, D. de Chambure, K. van Katwijk, D. Labergerie, U. Lienert, N. Schulz, "X-ray characterization of an XMM mandrel at the European Synchrotron Radiation Facility", SPIE Proc. 2515, p. 70, 1995.

20 B.L. Henke, E.M Gullikson E.M., J.C Davis, Atomic Data and Nuclear Data Tables, Vol.54, 1993.